Disrupted *Cacna1c* gene expression perturbs spontaneous Ca^{2+} activity causing abnormal brain development and increased anxiety

Erik Smedler[a,b,1], Lauri Louhivuori[a], Roman A. Romanov[c,d], Débora Masini[c], Ivar Dehnisch Ellström[a], Chungliang Wang[e], Martino Caramia[c], Zoe West[a], Songbai Zhang[a], Paola Rebellato[a], Seth Malmersjö[a], Irene Brusini[e,f], Shigeaki Kanatani[a], Gilberto Fisone[c], Tibor Harkany[c,d], and Per Uhlén[a,1]

[a]Department of Medical Biochemistry and Biophysics, Karolinska Institutet, Stockholm SE-17177, Sweden; [b]Department of Neuroscience and Physiology, Gothenburg University, Gothenburg SE-41345, Sweden; [c]Department of Neuroscience, Karolinska Institutet, Stockholm SE-17177, Sweden; [d]Department of Molecular Neurosciences, Centre for Brain Research, Medical University of Vienna, Vienna A-1090, Austria; [e]Department of Biomedical Engineering and Health Systems, KTH Royal Institute of Technology, Huddinge SE-14152, Sweden; and [f]Department of Neurobiology, Care Sciences and Society, Karolinska Institutet, Huddinge SE-14183, Sweden

Edited by Hee-Sup Shin, Center for Cognition and Sociality, Institute for Basic Science, Daejeon, South Korea; received May 11, 2021; accepted December 22, 2021

The L-type voltage-gated Ca^{2+} channel gene *CACNA1C* is a risk gene for various psychiatric conditions, including schizophrenia and bipolar disorder. However, the cellular mechanism by which *CACNA1C* contributes to psychiatric disorders has not been elucidated. Here, we report that the embryonic deletion of *Cacna1c* in neurons destined for the cerebral cortex using an *Emx1-Cre* strategy disturbs spontaneous Ca^{2+} activity and causes abnormal brain development and anxiety. By combining computational modeling with electrophysiological membrane potential manipulation, we found that neural network activity was driven by intrinsic spontaneous Ca^{2+} activity in distinct progenitor cells expressing marginally increased levels of voltage-gated Ca^{2+} channels. MRI examination of the *Cacna1c* knockout mouse brains revealed volumetric differences in the neocortex, hippocampus, and periaqueductal gray. These results suggest that *Cacna1c* acts as a molecular switch and that its disruption during embryogenesis can perturb Ca^{2+} handling and neural development, which may increase susceptibility to psychiatric disease.

Cacna1c | calcium signaling | brain development | psychiatric disorders | anxiety

Bipolar disorder and schizophrenia are severe mental disorders with significant morbidity and mortality that are associated with considerable societal costs (1, 2). Interestingly, there is a strong genetic association between schizophrenia and bipolar disorder, as indicated in large population-based studies (3). Genome-wide association studies have detected several single-nucleotide polymorphisms at a genome-wide significance level (4, 5). In combined studies on bipolar disorder and schizophrenia, *CACNA1C*, among several other genes, was concluded to be a risk gene (6, 7). By studying common genetic underpinnings common to autism spectrum disorder, attention deficit-hyperactivity disorder, bipolar disorder, major depressive disorder, and schizophrenia, the Psychiatric Genomics Consortium identified common risk loci that included single-nucleotide polymorphisms within *CACNA1C* and *CACNB2* (8, 9). Although it is clear that disturbances in *CACNA1C* expression play an essential role in the pathogenesis of several psychiatric disorders (10–12), the underlying cellular mechanism and its consequences on the developing and adult brain are poorly understood.

CACNA1C encodes the pore-forming α1c subunit of the L-type voltage-gated Ca^{2+} channel (VGCC) $Ca_v1.2$, which increases the cytosolic concentration of calcium ions (Ca^{2+}) upon strong depolarization (13). The channel is thought to play an important role in excitation-transcription coupling, neuronal survival, and synaptic efficacy (14–16). Ca^{2+} is a highly versatile second messenger involved in diverse processes such as oocyte fertilization (17), cell death via apoptosis (18), and brain development (19). In some instances, the cytosolic Ca^{2+} concentration starts to oscillate spontaneously, carrying information in the frequency of its oscillations (20, 21). In the developing neural circuits of the retina, cochlea, spinal cord, cerebellum, hippocampus, and neocortex, spontaneous activity has been reported to play an important role in the development of neurons and neural circuits (19, 22–24). Many different mechanisms for the generation of activity have been proposed in different systems, including the depolarizing action of GABA (as opposed to the traditional inhibitory effect due to the differential expression of chloride transporters), the formation of transient synaptic connections, and the presence of pacemaker-like neurons (25–27). In neural progenitors derived from mouse embryonic stem (ES) cells, spontaneous Ca^{2+} activity emerges early during differentiation prior to synaptogenesis (23, 28, 29). This spontaneous activity depends on extracellular Ca^{2+}, VGCCs (most likely both L- and T-type), and gap junctions and promotes proliferation and differentiation (28, 29).

Significance

The gene *CACNA1C* encodes for a calcium channel that has been linked to various psychiatric conditions, including schizophrenia and bipolar disorder, through hitherto unknown cellular mechanisms. Here, we report that deletion of *Cacna1c* in neurons of the developing brain disrupts spontaneous calcium activity and causes abnormal brain development and anxiety. Our results indicate that marginally alterations in the expression level of *Cacna1c* have major effects on the intrinsic spontaneous calcium activity of neural progenitors that play a crucial role in brain development. Thus, *Cacna1c* acts as a molecular switch that can increase susceptibility to psychiatric disease.

Author contributions: E.S., G.F., T.H., and P.U. designed research; E.S., L.L., R.A.R., D.M., I.D.E., M.C., Z.W., S.Z., P.R., S.M., I.B., and S.K. performed research; E.S., L.L., R.A.R., D.M., C.W., M.C., Z.W., I.B., and S.K. analyzed data; and E.S., L.L., and P.U. wrote the paper.

The authors declare no competing interest.

This article is a PNAS Direct Submission.

[1]To whom correspondence may be addressed. Email: erik.smedler@gu.se or per.uhlen@ki.se.

This article contains supporting information online at http://www.pnas.org/lookup/suppl/doi:10.1073/pnas.2108768119/-/DCSupplemental.

Published February 8, 2022.

Here, we examine the mental-disorder susceptibility gene *Cacna1c* and its role in brain development and adult behavior in mice. We combined knockout mice, behavioral assays, and brain imaging with computational modeling in conjunction with Ca^{2+} imaging, patch-clamp electrophysiology, and RT-qPCR screening to investigate how the molecular levels of *Cacna1c* in single cells can stimulate large-scale network activity in differentiating neural cells and can lead to abnormal development of the brain. Our findings reveal that disruption of *Cacna1c* perturbs spontaneous Ca^{2+} activity in neural progenitors, affecting cerebral cortical development and causing anxiety in adulthood.

Methods

Mouse Model. Forebrain-specific knockdown of *Cacna1c* was achieved by mating *Cacna1c* floxed mice (Jackson Stock 024714) with Emx1-IRES-Cre knockin mice (Jackson Stock 005628). Mice were group-housed and received food and water ad libitum under 12-h light–dark cycle conditions. All experiments were approved by Stockholm's Ethical Committee North (ethical approval N 40/15 and N 47/13). Genotyping was performed as described by Jackson.

Behavior Experiments. Anxiety-like behavior was assessed in adult (3- to 5-mo–old) wild-type (WT) and knockout (KO) male mice using the open-field test and elevated plus maze (8 mice/group) (30, 31). Experimental mice were housed in the same room as where the experiments were performed and were taken care of by the experimenter to acclimatize. The mice were tested during the light phase, and testing order was randomly determined to reduce time-of-day effects. The experimenter was blinded throughout the procedure. During the experiments, mice were first placed in the open-field arena for 10 min and, 7 d later, tested in the elevated plus maze for 5 min. Following each test, mice were removed and returned to a waiting home cage, and the maze was cleaned with soapy water followed by 70% ethanol. Upon finishing an experimental round, mice were regrouped according to original mixed-cage groups. Behavior experiments were recorded (30 fps) for later analysis. Assessment of behavior was done with an automated tracking system (Ethovision XT-11, Noldus). After completing the experimental procedures, some of the mice were prepared for MRI and killed.

Open field. The open-field test was run in a featureless square box (45 × 45 × 40 cm) made of gray Plexiglas. Mice were placed in the center of the chamber and left to explore for 10 min. Exploratory pattern was analyzed in bins of 5 min. The arena was divided into two equivalent areas: a central zone and the peripheral zone defined by its proximity to the walls. In this test, the preferential exploration of the peripheral zone of the open field is considered an index of anxiety.

Elevated plus maze. The elevated plus maze consisted of two open arms (30 × 6 cm, surrounded by a 0.5-cm high border) and two closed arms (30 × 6 cm, surrounded by 15-cm high walls) with two pairs of identical arms, which emerged from a central platform (6 × 6 cm), positioned opposite to each other. The platform was made of gray Plexiglas and elevated 45 cm above the floor. The test was initiated by placing the mouse on the central platform facing the open arm away from the experimenter. Each session lasted 5 min. The elevated plus maze relies upon rodents' proclivity toward dark, enclosed spaces and an unconditioned fear of heights/open spaces (32). Notably, the center zone of the elevated plus maze represents a conflict situation generated by opposite motivational states: approach to a new environment versus aversion to an open space. As a complementary measure of anxiety, the frequency of head dips was analyzed (downward movement of rodents' head toward the floor initiated when the body center is in the open arms or as a stretch-attend posture initiated from the central area of the maze). Head dips, together with time in center zone, represent measures for risk assessment behavior, showing considerable similarity to the apprehensive expectation and vigilance observed in generalized anxiety reactions (33).

Magnetic Resonance Imaging.

Fixation. To increase the signal/noise ratio and reduce the effective longitudinal relaxation time (T1) in the MRI, mice were perfused using the active staining technique (34), in which a contrast agent is used in conjunction with perfusion fixation. Mice were sedated by intraperitoneal injection of ketamine (Ketaminol vet solution from Intervet, 50 mg/kg) and xylazine (Rompun vet solution from Bayer Animal Health, 50 mg/kg). Systemic perfusion was performed via the right jugular vein and the left carotid artery with a perfusion pump (MINIPULS 3 Peristaltic pump; Gilson Inc.) at 0.5 mL/min (24 rpm). Vasculature was first flushed with 25 mL phosphate-buffered saline (PBS) at room temperature and thereafter perfused with 20 mL of 4% Histofix (Histofix 4%; Histolab) containing 10% gadoteridol (Prohance solution for injection 279.3 mg/mL, 50 mM; Bracco Sweden). After perfusion, heads were removed and cleaned from skin, eyes, mandible, muscles, and teeth. Next, heads were immersed in 4% Histofix containing 1% gadoteridol for 24 h at 4 °C. Heads were transferred to 0.1 M PBS containing 1% gadoteridol at 4 °C for 7 d. The final step of rehydration in PBS minimized shrinkage or swelling.

Ex vivo MRI. Six anonymized and gadolinium-enhanced *Cacna1c* KO ($n = 3$) and WT ($n = 3$) mouse heads were wrapped in gauze and fitted in a 30-mL plastic syringe filled with Fomblin (Solvay Solexis) to minimize susceptibility artifacts at interfaces and to provide a stable position with a dark background. The syringe was positioned in a millipede coil with an inner diameter of 30 mm and scanned overnight in a 9.4 T horizontal bore MRI scanner (Agilent). Spin-echo three-dimensional (3D) data were acquired overnight (recovery time 140 ms, echo-time 11.31 ms, field-of-view 62 × 31 × 31 mm^3, matrix 1024 × 512 × 512), resulting in a total scan duration of 10 h and 12 min. It may be noted that the resulting images are mainly transverse relaxation time weighted, as the T1 is shortened to <100 ms by the gadolinium treatment.

Image analysis. All brain MRI images were parcellated by performing atlas-based segmentation using the Waxholm Space mouse atlas (35). The NiftyReg package that implements a normalized mutual information-based registration method was used to perform the deformable registration (36). All nerve bundles were excluded from the statistical analysis because the cutting points were not consistent. The regional brain volumes were normalized to the whole brain volume. For mammillary bodies, a trained radiologist performed manual segmentation.

Cortex Imaging in Brain Slices.

Slice preparation and cortex layer imaging. Mouse head samples used for MRI experiments were stored in MilliQ water until use. The skin of the heads was removed, and skull decalcified with 20% ethylenediaminetetraacetic acid solution at 37 °C for 4 d with rotation. After collecting the brains, the samples were incubated in 30% sucrose/PBS solution three times until the samples sank. The samples were then coronally cut in half using Mouse Brain Matrices (AgnTho's) and embedded in Tissue-Tek Optimal Cutting Temperature compound (SAKURA Finetek). Coronal cryosections were cut in 14-μm thickness. Antigen retrieval was then performed on the brain sections with HistoVT One (1×; Nacalai Tesque, Inc.) at 95 °C for 20 min. The sections were then washed with PBS + 0.05% Triton × 100 (PBS-Tx) and blocked with blocking reagent (PerkinElmer) in PBS for 1 h at room temperature (RT). Sections were incubated with primary antibodies, Ctip2 (1/200, rat; Abcam ab18465), Satb2 (1/100, mouse; Abcam ab51502), and Tbr1 (1/200, rabbit; Abcam ab31940) overnight at 4 °C. Following primary antibody incubation, the brain sections were washed three times with blocking solution and incubated for 1 h at RT with secondary antibodies donkey anti-rabbit Alexa 488, donkey anti-rat DyLight 550, and donkey anti-mouse Alexa 647 (all from Invitrogen) in blocking solution. Nuclei were stained with DAPI (5 μg/mL; Molecular Probes) for 1 h. Sections were then washed with blocking solution three times and mounted.

Image acquisition. Slices were imaged with a confocal microscope (Zeiss LSM900-Airy; Carl Zeiss) equipped with a plan-apochromat 20×/0.8 ∞/0.17 objective lens (Carl Zeiss). All images were acquired at the somatosensory cortex by using the position of the hippocampus as a landmark.

Cortex layer analysis. Each layer thickness was measured in ImageJ using layer markers and DAPI signal. For comparisons between layers, two-sided unpaired *t* tests were used.

Simulations. The coupled ordinary differential equations (ODEs) were implemented and integrated in MATLAB (The MathWorks) using the built-in ODE solver ODE15s. See the *SI Appendix* for details.

ES Cell Differentiation. Mouse ES cells were differentiated as described previously (37). Briefly, pluripotent cells of the R1 strain were seeded onto gelatin-coated dishes and cultured in neural induction medium with N2 and B27 without leukemia inhibitory factor.

Molecular Biology. RNA was collected at different stages of differentiation (0, 2, 4, 6, 8, and 10 d for time course or day 4 and 8 for screening). For the time course study, total RNA was extracted using the RNeasy kit (Qiagen), and reverse transcription was conducted with a SuperScript II reverse transcriptase (Invitrogen) according to the manufacturer's protocol. Real-time PCR primers were as follows: connexin-43 (*Gja1*) forward TTTGACTTCAGCCTCCAAGG, reverse CCATGTCTGGGCACCTCT; $Ca_v1.2$ (*Cacna1c*) forward CGTTCTCATCC TGCTCAACA, reverse TATGCTCCCAATGACGATGA; TATA-box binding protein (*Tbp*) forward GGGGAGCTGTGATGTGAAGT, reverse CCAGGAAATAATTCT GGCTCA; βIII-tubulin (*Tubb3*) forward CATGGACAGTGTTCGGTCTG, reverse TGCAGGCAGTCACAATTCTC. The $2^{-\Delta CT}$ values were used to calculate the relative expression levels compared to *Tbp* and are given as the mean ± SEM. For

the mouse neuronal ion channel screen, total RNA was extracted and transcribed to cDNA using an RT^2 Profiler First Strand Kit (Qiagen). Real-time PCR primers were supplied in the RT^2 Profiler PCR Array PAMM-036Z (Qiagen). RT^2 SYBR Green ROX qPCR Mastermix (Qiagen) was used for the qPCR run. The $2^{-\Delta CT}$ values were used to calculate the relative expression levels compared to the norm and are given as the mean ± SEM. Only genes with $C_T < 35$ for all replicates were used for further analysis (72 of a possible 84). The norm was calculated as the geometric mean of five housekeeping genes: *Actb*, *B2m*, *Gapdh*, *Gusb*, and *Hsp90ab1* (38).

Calcium Imaging. Cells were loaded with the Ca^{2+}-sensitive fluorescence indicator Fluo-3/AM (5 μM; Invitrogen) at 37 °C for 30 min in Krebs-Ringer buffer containing 119.0 mM NaCl, 2.5 mM KCl, 2.5 mM $CaCl_2$, 1.3 mM $MgCl_2$, 1.0 mM NaH_2PO_4, 20.0 mM Hepes (pH 7.4), and 11.0 mM dextrose. Measurements of cytosolic Ca^{2+} were carried out in Krebs-Ringer buffer at 37 °C using a heat-controlled chamber (QE-1; Warner Instruments) and a cooled electron-multiplying charged-coupled camera (QuantEM 512SC; Photometrics) mounted on an upright fixed stage microscope (Axio Examiner.A1; Carl Zeiss) equipped with a 20× 1.0 NA objective lens (Carl Zeiss). Excitation at 480 nm was assessed with an illumination system (DG4; Sutter Instrument). MetaFluor (Molecular Devices) was used to control all devices and to analyze acquired images. The overall changes in Ca^{2+} concentration was determined using MATLAB (The MathWorks). An active cell had two Ca^{2+} transients or more at least 10% above baseline. Frequency was calculated by dividing the number of transients with duration. The time duration for individual Ca^{2+} peaks was analyzed by calculating the full duration at half maximum (FDHM). Briefly, the FDHM value for a Ca^{2+} peak is given by the time difference between the two points on each side of the peak where the value is half of the maximum value. Network analysis was performed as described recently (39) with the same cutoff (0.39) as previously defined (28). Normalized overlap between putative pacemaker cells and hub cells was calculated by dividing the number of overlapping cells by the total number of pacemaker cells. Gap junctions were inhibited with 1 mM octanol (Sigma-Aldrich), sarco/endoplasmic reticulum Ca^{2+}-ATPase (SERCA) with 1 μM thapsigargin (Invitrogen), and ryanodine receptors (RyR) with 10 μM ryanodine (Tocris).

Calcium Imaging in Brain Slices.

Slice preparation and Ca^{2+} imaging. Neocortical slices were prepared from mouse pups at postnatal day 7. Briefly, after brain extraction, 300-μm coronal slices were cut perpendicular to the pial surface with a vibratome (VT1000S; Leica) in ice-cold modified artificial cerebrospinal fluid (ACSF) containing the following: 125 mM NaCl, 25 mM $NaHCO_3$, 1.25 mM NaH_2PO_4, 20 mM glucose, 2.5 mM KCl, 1 mM $CaCl_2$, 8 mM $MgCl_2$. After being allowed to rest for at least 1 h in oxygenated ACSF containing 125 mM NaCl, 25 mM $NaHCO_3$, 1.25 mM NaH_2PO_4, 20 mM glucose, 5 mM KCl, 2 mM $CaCl_2$, and 1 mM $MgCl_2$ at RT, slices were transferred to a custom-made oxygenated loading chamber, where they were bulk loaded with Fluo-4/AM (30 μM; Invitrogen) and 0.07% Pluronic F-127 (Invitrogen) at 37 °C for 30 to 40 min. Slices were then allowed to rest and rinse in ACSF at RT for least 30 min before being placed into the acquisition chamber and imaged with a 2-photon laser-scanning microscope (2PLSM, Zeiss LSM 510 NLO; Carl Zeiss) equipped with a Coherent Chameleon Ultra II Titanium-sapphire pulsed laser (Coherent, Inc.) and a plan-apochromat 20× 1.0 NA water immersion objective lens (Carl Zeiss). Slices were held in place with a nylon mesh grid (Warner Instruments), and oxygenated ACSF (at RT) was perfused into the chamber continuously during the experiments.

Image acquisition and analysis. All images were acquired at a tissue depth of at least 30 μm. Fluo-4/AM was excited at 910 nm, and emission light was spectrally filtered by a 510- to 600-nm bandpass filter. A sequence of 16-bit single z-plane images was acquired at a 512 × 512-pixel resolution with the sampling frequency 0.5 Hz (every 2 s) under the control of the Zeiss Zen2009 software (Carl Zeiss). Custom in-house MATLAB scripts and ImageJ were used to analyze the data. The Fourier-transform spectral analysis of Ca^{2+} oscillations was performed as described elsewhere (40).

Electrophysiology. Neural progenitors were recorded with the patch-clamp technique using the whole-cell configuration. Ion currents (voltage-clamp mode) and membrane potentials (current-clamp mode) were recorded, filtered, and analyzed using an Axopatch 200 B amplifier, a DigiData1322 interface, and the pClamp10 software (Molecular Devices). Intracellular solution contained 114 mM potassium gluconate, 6 mM KCl, 10 mM Hepes, 5 mM ethylene glycol tetraacetic acid, 4 mM ATP-Mg, and 0.3 mM guanosine triphosphate. The pH was adjusted to 7.3 with KOH. The bath solution for electrophysiological recordings contained 140 mM NaCl, 2.5 mM KCl, 1 mM $MgSO_4$, 1.3 mM $CaCl_2$, 1.2 mM NaH_2PO_4, 10 mM glucose, and 10 mM Hepes-NaOH (pH 7.4). In pharmacological experiments, L-type voltage-gated Ca^{2+} channel-like currents were probed with nifedipine (5 μM) superfused in the bath solution.

Statistics. Experimental values are presented as means ± SEM unless stated to be approximate (~). Independent biological replicates are denoted by *N*, number of independent experiments, and *n*, number of cells. For comparisons between two groups, two-sided unpaired *t* tests (parametric) or Mann-Whitney *u* tests (nonparametric) were used. For statistical analyses of Ca^{2+} imaging experiments, two-sided unpaired *t* tests and *N* as biological replicant were used. For the ion channel screen and MRI analysis, *P* values were adjusted for multiple comparisons using the false discovery rates (FDRs), and the thresholds 0.05 and 0.1, respectively, were used. For correlations analysis, the Pearson's method was used. For open-field tests, a two-way ANOVA with repeated measures was used to assess the effect of time bin and genotype, and when significance was detected, a Bonferroni multiple comparison test was performed. For principal component analysis, the pca function in MATLAB R2018 (The MathWorks) was used. Statistical tests were performed in MATLAB (The MathWorks), Microsoft Excel version 15/16 (Microsoft Corporation), and GraphPad Prism 8/9 (GraphPad Software). Differences were considered significant at $*P < 0.05$, $**P < 0.01$, and $***P < 0.001$ and nonsignificant (ns) at $P > 0.05$.

Results

***Cacna1c* Modulates Spontaneous Ca^{2+} Activity in Brain Slices.** To explore the impact of *Cacna1c* disruption on brain development, we first set out to generate forebrain-specific (41) KO mice by mating *Cre-Emx1* mice with *loxP-Cacna1c* mice. Since *Cacna1c* encodes the α1c subunit of the L-type VGCC, we hypothesized that *Cacna1c* KO mice might have altered Ca^{2+} handling. We performed 2-photon laser-scanning Ca^{2+} imaging of single neural progenitors in neocortical layers II to VI of the WT and KO mice at postnatal day 7. Cells in the neocortex displayed spontaneous Ca^{2+} activity in both the WT (Fig. 1*A*) and KO (Fig. 1*B*) mice; however, the amplitude of the oscillating Ca^{2+} waves appeared lower in the KO brain slices. A pooled analysis of all detected Ca^{2+} spikes revealed significantly higher amplitudes in neural progenitors from WT mice compared to those from KO mice (Fig. 1*C*; WT: $n = 1{,}857$, $N = 5$; KO: $n = 1{,}160$, $N = 4$; $P < 0.001$, *t* test). We next performed a Fourier-transform–based spectral analysis of the Ca^{2+} oscillation frequency in spontaneously active neural progenitor cells. The results showed no significant frequency difference between the WT and KO mice (Fig. 1*D*; WT: 13.1 ± 0.5 mHz, $n = 177$, $N = 5$; KO: 12.9 ± 1.2 mHz, $n = 41$, $N = 4$; $P = 0.87$, *t* test). However, the number of cells displaying spontaneous Ca^{2+} activity was significantly higher in the WT mice than in the KO mice (Fig. 1*E*; WT: $n = 297$, $N = 5$; KO: $n = 54$, $N = 4$; $P = 0.0037$, *t* test). Together, these data reveal that the disruption of *Cacna1c* perturbs spontaneous Ca^{2+} activity in neocortical neural progenitors during development.

High *Cacna1c* Expression in Neural Progenitors with Spontaneous Ca^{2+} Activity. We previously reported that differentiating mouse ES cells start to exhibit spontaneous Ca^{2+} activity at days 6 to 8 (29). To identify important gene expression changes within this time window of neural differentiation, we set up an RT-qPCR screen for the differential expression of genes encoding 84 different neuronal ion channels. RNA was collected from the neural progenitors and compared between day 4 and day 8 ($n = 3$). The fold-changes and *P* values for the comparisons revealed that the four most significantly up-regulated genes all encoded subunits of VGCCs (Fig. 1*F*). Interestingly, *Cacna1c*, which encodes the α1c subunit of $Ca_v1.2$, was up-regulated 33.8-fold (Fig. 1*G*), whereas *Cacng2* and *Cacng4*, which encode the γ2 and γ4 subunits of the L-type VGCC (Fig. 1*H*), were up-regulated 33.0- and 5.9-fold, respectively. *Cacna1d*, which encodes the α1d subunit of $Ca_v1.3$, showed no difference, with a fold-change of 1.04, and *Cacnb3*, which encodes the β3 subunit of L-type VGCC, was up-regulated 2.2-fold.

NEUROSCIENCE

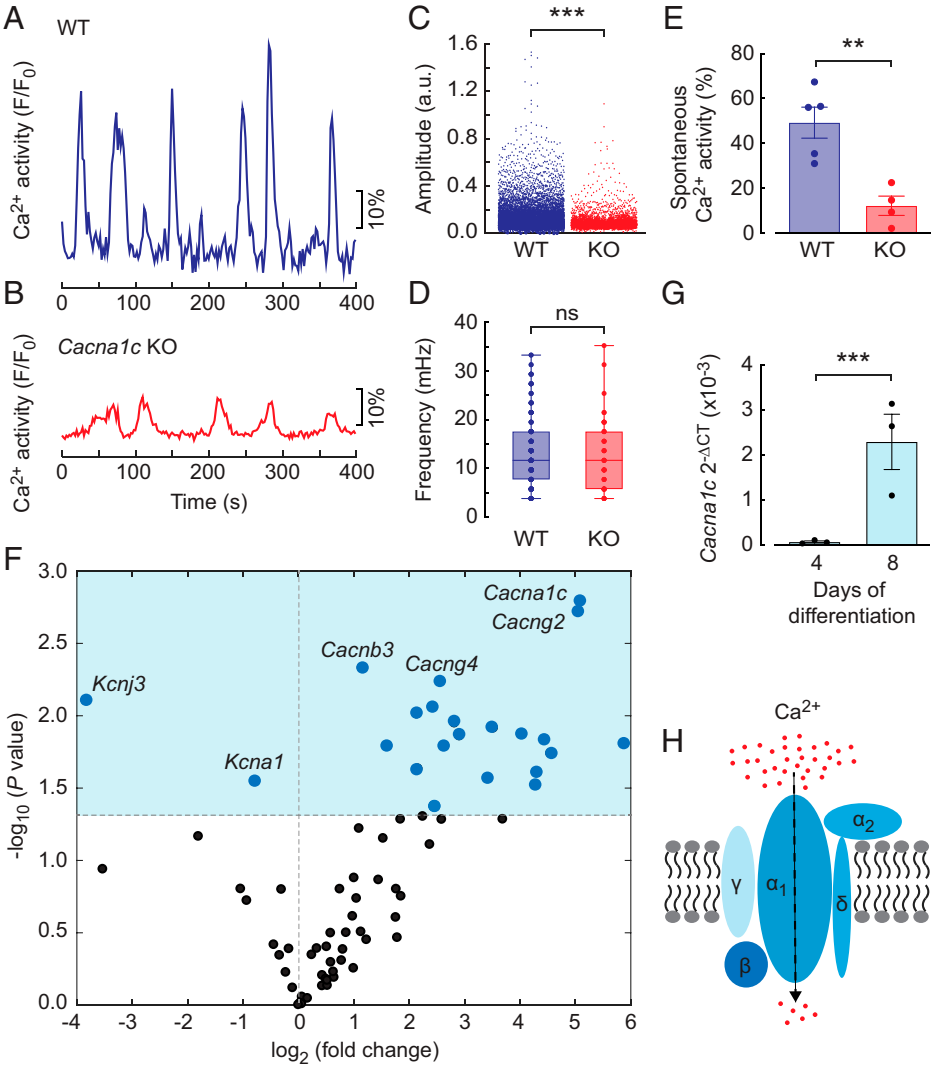

Fig. 1. *Cacna1c* expression increases on day 8 of ES cell differentiation and perturbs the Ca^{2+} spike amplitude in KO mice. (*A* and *B*) Single-cell Ca^{2+} traces from the WT (*A*) and *Cacna1c* KO (*B*) mouse brain slices. (*C* and *D*) Spike amplitude (*C*) and oscillatory frequency (*D*) of the spontaneous Ca^{2+} activity in cells from the WT and *Cacna1c* KO brain slices. For the box plots, the center line shows the median, the upper and lower boundaries of the box show the upper and lower quartiles, and the whiskers show the minimum and maximum values. (*E*) Percentage of cells with spontaneous Ca^{2+} activity from the WT and *Cacna1c* KO brain slices. (*F*) Volcano plot of the differentially expressed genes encoding 84 different ion channels at days 4 and 8 of ES cell differentiation. The dark-blue dots indicate reduced and increased gene expression, and the light-blue area indicates $P < 0.05$ after FDR correction. (*G*) *Cacna1c* mRNA expression levels at days 4 and 8 of ES cell differentiation. (*H*) Schematic representation of the VGCC subunits. The bars are the mean ± SEM. The *P* values for the volcano plot and significance tests were calculated using unpaired two-tailed *t* tests. $^{**}P < 0.01$, $^{***}P < 0.005$; ns, nonsignificant ($P > 0.05$). a.u., arbitrary unit.

The remaining genes with significantly altered expression identified by the RT-qPCR screen encoded mainly subunits of potassium and sodium channels.

Spontaneous Ca^{2+} Activity in Neural Progenitors Can Be Computationally Modeled. Differentiating cells are highly heterogeneous in their levels of gene expression (29, 42, 43). To assess the effect of subtle differences in gene expression levels in single cells on spontaneous oscillations, we developed a computational model based on three interconnected cells expressing essential ion channels and pumps that control the cytosolic Ca^{2+} concentration (Fig. 2*A*; *SI Appendix*). The model included VGCCs that mimicked high voltage-activated L-type Ca^{2+} channels (*SI Appendix*, Fig. S1*A*). We first tested two realistic VGCC conductance values that differed only slightly, 20.0 μS/cm^2 and 17.5 μS/cm^2. Both values produced persistent spontaneous Ca^{2+} oscillations of similar amplitude and frequency (Fig. 2 *B* and *C*). Interestingly, upon gap junction blockade ($g/v_{gap} = 0$), the cell with the marginally higher VGCC conductance (20 μS/cm^2) continued to oscillate (Fig. 2*B*), whereas the cell with the marginally lower VGCC conductance (17.5 μS/cm^2) stopped oscillating (Fig. 2*C*). Notably, in the cell that remained active after blocking gap junctions, the FDHM of each Ca^{2+} transient increased 125%, from 67 s to 151 s, and the frequency decreased 24%, from 5.9 mHz to 4.5 mHz. Assessment of the membrane potential in these cells revealed that the oscillating membrane potential was driving the oscillation of the cytosolic Ca^{2+} concentration (Fig. 2 *D*–*F*). Such membrane potential dynamics are typical of the Morris-Lecar model, which represents a relaxation oscillator with push and pull forces (44). As expected, the dynamics of the endoplasmic reticulum (ER) Ca^{2+} concentration was the opposite of those of the cytosolic Ca^{2+} concentration (Fig. 2*G*; *SI Appendix*, Fig. S1 *B*–*D*). To test the computational model against experimental data, we compared the computational data with Ca^{2+} recordings from

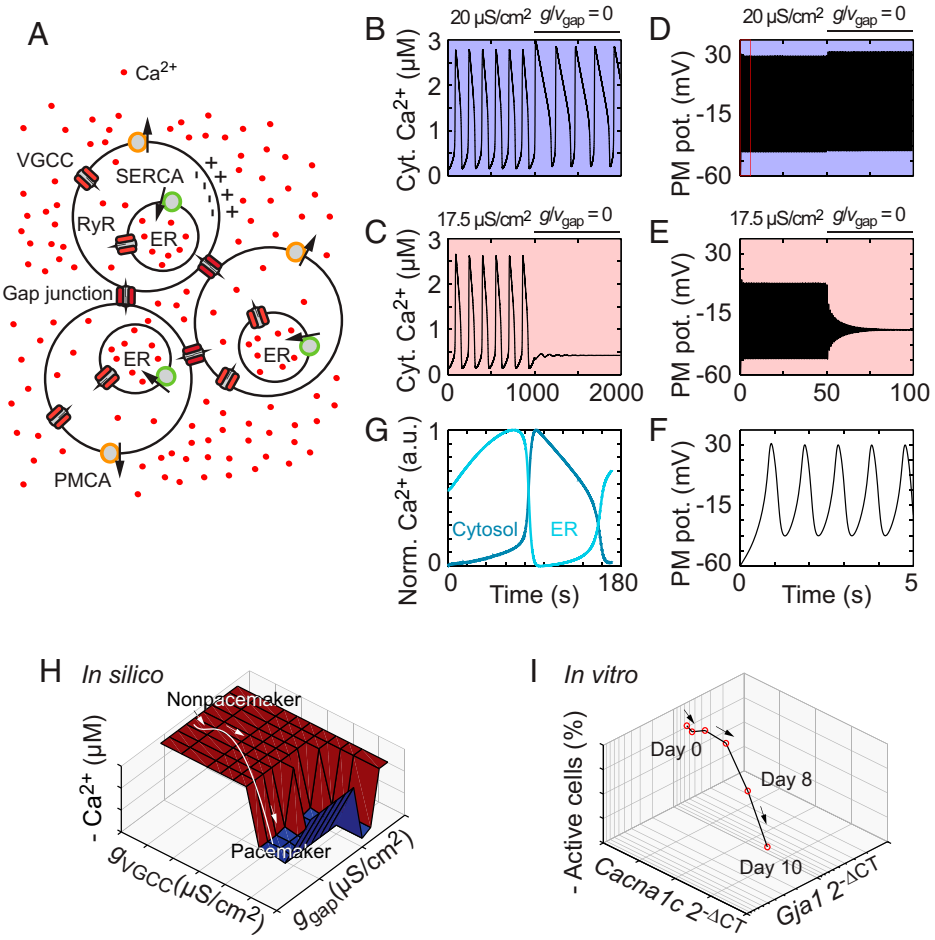

Fig. 2. Computational modeling reveals the critical roles of VGCC in pacemaker cells and gap junctions in nonpacemaker cells. (*A*) Schematic view of three interconnected cells. The Ca^{2+} concentration and membrane potential are modeled in each individual cell. (*B–E*) Computational modeling of the cytosolic Ca^{2+} concentration (*B* and *C*) and membrane potential (*D* and *E*) at conductances of 20 μS/cm^2 (*B* and *D*) and 17.5 μS/cm^2 (*C* and *E*). (*F*) Zoomed-in time course of 5 s from *D* (boxed region) with five membrane potential oscillatory periods. (*G*) The ER Ca^{2+} concentration (light blue) versus the cytosolic Ca^{2+} concentration (dark blue). (*H*) Bifurcation analysis with the gap junction and VGCC conductances, g_{gap} and g_{VGCC}, respectively, as bifurcation parameters. The values are g_{gap} (*x*-axis), g_{VGCC} (*y*-axis), and the negative oscillation amplitude (*z*-axis). (*I*) Trajectory of differentiating ES cells based on the RT-qPCR measurements of *Cacna1c* and *Gja1*. The values are the mean expression levels of the connexin-43 gap junction gene *Gja1* (*x*-axis), the $Ca_v1.2$ subunit gene *Cacna1c* (*y*-axis), and the mean number of oscillating cells (*z*-axis) at days 0 to 10 of differentiation. Computational data are indicated in silico, and experimental data from differentiating cells are indicated in vitro. Cyt., cytosolic; PM, plasma membrane; pot., potential; a.u., arbitrary unit.

neural progenitors exposed to inhibitors of RyR, VGCC, and SERCA. Intriguingly, the cell kinetics in our computational model showed strong similarities with those of the stem cell–derived neural progenitors (*SI Appendix*, Fig. S2).

Bifurcation Analysis of Gap Junctions and VGCC Conductance. We then performed a bifurcation analysis to gain further insight into the role of gap junctions and VGCCs in promoting the oscillatory behavior of the cytosolic Ca^{2+} concentration. A bifurcation occurs in the event of a sudden change in the activity of a dynamic system, such as the transition from nonoscillatory to oscillatory behavior (45). First, we chose to use the gap junction conductance (g_{gap}) as a bifurcation parameter while keeping the VGCC conductance constant and the gap junction Ca^{2+} permeability at zero. Spontaneous Ca^{2+} transients emerged at a Hopf bifurcation (*SI Appendix*) at approximately g_{gap} = 0.04 μS/cm^2 (*SI Appendix*, Fig. S3 *A* and *B*). Notably, in vivo experiments on neural progenitors have shown that the gap junction conductance is ~10^4 μS/cm^2 (28), which is safely within the oscillatory regime of our model. We next treated the VGCC conductance (g_{VGCC}) as a bifurcation parameter while keeping the gap junction conductance and Ca^{2+} permeability constant. An oscillatory regime occurred bounded by two Hopf bifurcations at g_{VGCC} = 18.0 μS/cm^2 and g_{VGCC} = 26.4 μS/cm^2 (*SI Appendix*, Fig. S3 *C* and *D*). Thus, the cells with the lower g_{VGCC}, e.g., 17.5 μS/cm^2, which was below the lowest bifurcation point, were not capable of evoking spontaneous Ca^{2+} transients, whereas the cells with the marginally higher g_{VGCC}, e.g., 20 μS/cm^2, could generate intrinsic spontaneous Ca^{2+} transients. These results, together with the analysis of RyR Ca^{2+} permeability as a bifurcation parameter (*SI Appendix*), confirm that the spontaneous Ca^{2+} oscillations in our model system are driven by membrane potential oscillations and not vice versa. Moreover, our data define two functionally distinct cell types, pacemakers and nonpacemakers, that either have or lack intrinsic spontaneous Ca^{2+} activity, respectively.

The Developmental Trajectory in the Parameter Space Is Analogously Realized in Experimental Data. To test how well our computational model predicted the real-world outcomes, we created a 3D space in which the *x*-, *y*-, and *z*-axes corresponded to the modeled and experimental values for gap junctions, VGCC, and spontaneous Ca^{2+} oscillations, respectively. Plotting the values for the g_{gap}, g_{VGCC}, and spontaneous Ca^{2+}

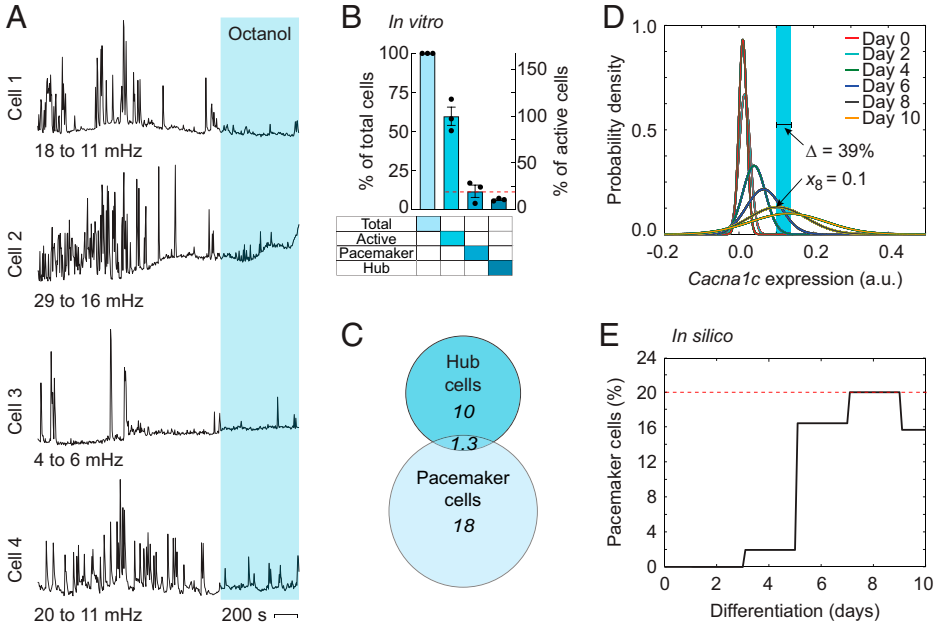

Fig. 3. Computationally predicted pacemaker cells can be confirmed experimentally. (*A*) Four single-cell Ca^{2+} recordings of putative pacemaker cells. The light-blue region indicates gap junction inhibition with octanol. (*B*) Histogram showing the percentage of total, active, pacemaker, and hub cells versus total cells (left *y*-axis) and active cells (right *y*-axis). (*C*) Venn diagram for the pacemaker cells and hub cells. (*D* and *E*) Modeled distribution of *Cacna1c* expression at different time points during differentiation (*D*) and the number of pacemaker cells as a function of days of differentiation (*E*). The red dashed lines indicate the percentage of pacemaker cells of active cells. The light-blue region indicates the oscillatory regime determined by the bifurcation window (Δ) and the *Cacna1c* RT-qPCR measurement at day 8 (x_8). Experimental data from neural progenitor cells are indicated in vitro and computational data are indicated in silico. The bars are the mean ± SEM. a.u., arbitrary unit.

oscillations generated by the computational model in the 3D space revealed an "oscillation pit" in which cells were prone to oscillate (Fig. 2*H*). We then plotted experimental values in the 3D space from measurements of RNA levels for the genes encoding the connexin 43 gap junction subunit (*Gja1*) and the α1c subunit of $Ca_v1.2$ (*Cacna1c*) as well as Ca^{2+} activity over 10 d of differentiation (Fig. 2*I*). There was a discrepancy between the expression trajectories of the two genes over time, wherein *Gja1* varied slightly while *Cacna1c* increased dramatically (*SI Appendix*, Fig. S4*A*). Intriguingly, the trajectory resulting from the experimental data followed the 3D surface plot created by the computational model, wherein cells on day 8 fell into the "oscillation pit" (Fig. 2*H*; *SI Appendix*, Fig. S4*B*). The number of cells displaying spontaneous Ca^{2+} activity on day 8 increased significantly to 18.5 ± 4.3% and on day 10 to 37.0 ± 1.5% (*SI Appendix*, Fig. S4*C*; Day 8: $n = 108$, $N = 4$, $P = 0.010$; Day 10: $n = 124$, $N = 4$, $P = 0.0029$; *t* tests). Notably, there was a high positive correlation between spontaneous Ca^{2+} activity and the expression levels of *Cacna1c* ($n = 6$, $P = 0.04$, Pearson's $r = 0.83$).

Pacemakers and Nonpacemakers. A functional classification of cells is the so-called pacemaker cell, which is recognized as a cell with intrinsic spontaneous activity (46, 47). We chose to define the putative pacemakers as neural progenitor cells that remained spontaneously Ca^{2+}-active after treatment with the gap junction blocker octanol (Fig. 3*A*). In total, 59 ± 1.9% ($n = 482$, $N = 3$) of the cells displayed spontaneous Ca^{2+} activity, of which 19 ± 5.1% ($n = 284$, $N = 3$) remained active after blocking gap junctions (Fig. 3*B*). Among the pacemaker cells, 13 ± 7.2% ($n = 30$, $N = 3$) were determined to be hub cells (Fig. 3 *B* and *C*), which are defined as cells with multiple network connections to other cells (39). We also analyzed the spatial distribution of the pacemaker and nonpacemaker cell populations and whether they were clustered together. This analysis showed no significant differences in spatial distribution and center of mass between the pacemakers and nonpacemakers (*SI Appendix*, Fig. S4 *D* and *E*). Intriguingly, assessing the frequency of intrinsic spontaneous Ca^{2+} oscillations in pacemaker cells revealed a significant decrease of 26 ± 8.8% ($n = 54$, $N = 3$, $P < 0.001$, *t* test) after blocking gap junctions with octanol (*SI Appendix*, Fig. S4*F*), consistent with our computational model, which showed a 24% decrease after gap junction inhibition (Fig. 2*B*). We next tested whether our computational model generated a percentage of pacemaker cells similar to that obtained by our experiments on neural progenitors. By assuming a Gaussian expression distribution for *Cacna1c* (Fig. 3*D*; *SI Appendix*), we performed a statistical assumption that predicted 20% pacemaker cells on day 8 (Fig. 3*E*). The percentage of pacemakers generated by the computational model closely matched the experimental data, which showed 19% oscillating neural progenitors (Fig. 3*B*).

Nonpacemaker Cells Can Be Converted to Pacemaker Cells. On the basis of our experimental and theoretical results, we hypothesized that the only difference between a pacemaker cell and a nonpacemaker cell is the VGCC conductance. Thus, we tested whether pacemaker and nonpacemakers cells could be transformed into each other by applying an outward or inward electrical current. Our bifurcation analysis predicted that the spontaneous activity of a pacemaker cell could be inhibited by applying an outward electrical current of 34 nA/cm^2 (corresponding to 0.43 pA for a spherical cell with a radius of 10 μm), whereas a nonpacemaker cell could be induced to start spiking by applying an inward current of 1 nA/cm^2 (corresponding to 0.013 pA) (Fig. 4*A*). While studying neural progenitors with consecutive recordings of cytosolic Ca^{2+} and electrical current, we tested our hypothesis by patching cells showing spontaneous Ca^{2+} activity. First, we confirmed that individual cells in our population of neural progenitors were spontaneously active (Fig. 4*B*) and excitable (*SI Appendix*, Fig. S5). Second, we concluded that L-type currents were indeed present, as part of the inward current was blocked by 5 μM nifedipine (Fig. 4*C*; *SI*

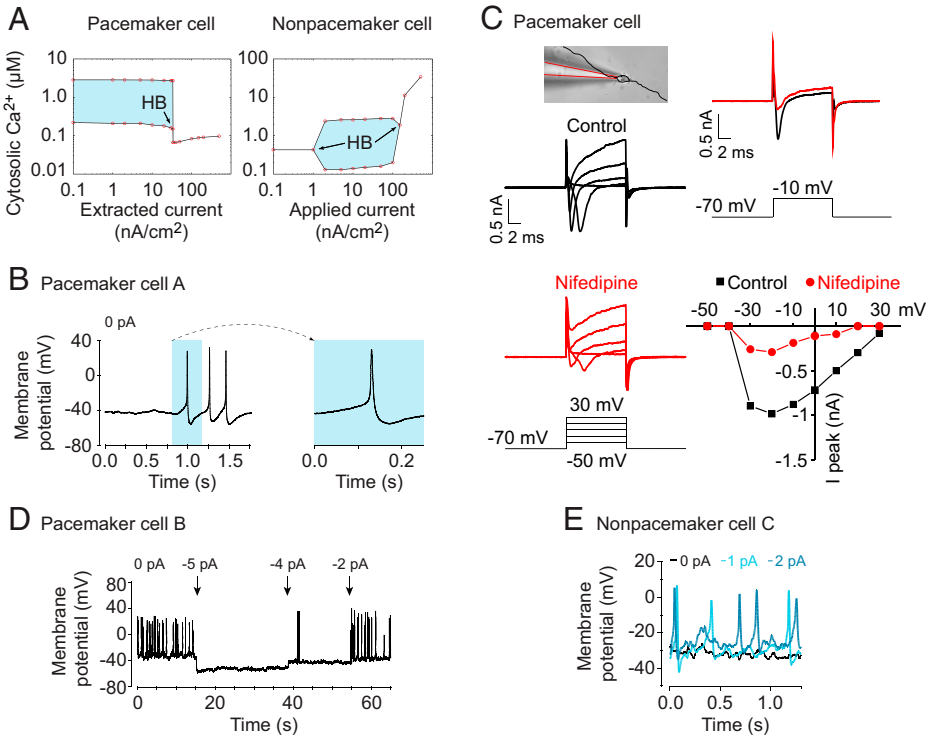

Fig. 4. Cells can switch between pacemaker and nonpacemaker state by altering the membrane potential. (*A*) Bifurcation analyses with extracted and applied electrical currents as bifurcation parameters in a pacemaker and nonpacemaker cell, respectively. Hopf bifurcations (HBs) at I_{app} = 1 nA/cm^2 and 200 nA/cm^2. (*B*) Action potentials in pacemaker cell A measured with patch-clamp recordings. (*C*) Ion current recordings (voltage-clamp mode) in a pacemaker cell in absence (Control) or presence of 5 μM nifedipine. (*Top Left*) Photomicrograph showing the cell with the patch pipette attached. Soma and processes are highlighted in black overlay. (*Bottom Left*) Voltage steps from −50 to +30 mV from −70 mV holding potential. (*Top Right*) Residual inward current upon a current step from −70 mV to −10 mV. (*Bottom Right*) Relationship between voltage and current. Peak conductance is seen at around −20 mV. (*D*) Spontaneous membrane potential activity in pacemaker cell B in which negative currents (−5, −4, and −2 pA) were applied. (*E*) Spontaneous membrane potential activity in nonpacemaker cell C in which positive currents (1 pA and 2 pA) were applied.

Appendix, Fig. S6). We then identified a putative pacemaker cell with a spontaneous activity that we transformed into a nonpacemaker cell by applying a small negative current of −5 pA, which completely abolished the spontaneous activity (Fig. 4*D*). Interestingly, raising the applied current to −2 pA reactivated the cell and returned it to the spontaneously active state. Thereafter, we patched into a nonpacemaker cell that lacked spontaneous activity. By applying small positive currents of 1 or 2 pA to this cell, we evoked spontaneous activity (Fig. 4*E*). One pA at −30 mV corresponds to 33.3 pS in an ohmic approximation, which corresponds to approximately one channel (assuming a spherical cell with a radius of 10 μm). Intriguingly, ∼33.3 pS was the difference between a nonpacemaker cell and a pacemaker cell in the computational model (*SI Appendix*, Fig. S3*D*). These results imply that the expression level of *Cacna1c* in neural progenitors can act as a molecular switch, determining whether the cell becomes a pacemaker or a nonpacemaker cell.

***Cacna1c* KO Mice Show Increased Anxiety.** Finally, we sought to investigate how *Cacna1c* knockdown in the cerebral cortex affected behavior and development. As a measure of anxiety-related behavior, adult WT (n = 8) and *Cacna1c* KO (n = 8) mice were subjected to the open-field test and the elevated plus maze test to assess their general locomotion, patterns of exploratory behavior, and instances of risk assessment behavior (Fig. 5*A*). In the open field, by comparing the first 5 min and last 5 min of the experiments, we observed significant evidence of behavioral inhibition in the *Cacna1c* KO mice, as characterized by the initial avoidance of novelty exploration compared to the exploration behavior of the WT mice (Fig. 5*B*). A two-way ANOVA was conducted for the influence of genotype and time bin, which showed significant interaction effects on distance (n = 8 mice per group, interaction $F_{1,14}$ = 43.42, P < 0.0001, two-way ANOVA), speed (n = 8 mice per group, interaction $F_{1,14}$ = 22.00, P = 0.0003, two-way ANOVA), and visits to the center (n = 8 mice per group, interaction, $F_{1,14}$ = 12.92, P = 0.0029, two-way ANOVA). For WT mice, the distance, speed, and visits to the center were found to decrease when the first 5 min was compared with the last 5 min (n = 8 mice per group; distance, P = 0.002; speed, P = 0.0076; visits to center, P = 0.0204; Bonferroni multiple comparison tests), as expected for a normal pattern of exploration followed by habituation to a novel environment. Intriguingly, for the KO mice, all three behavioral parameters increased with time, two of them significantly (n = 8 mice per group; distance, P = 0.0031; speed, P = 0.0136; visits to center, P = 0.105; Bonferroni multiple comparison tests). This behavior is indicative of a reduced exploratory drive upon initial exposure to novelty, which can be interpreted as a higher state of anxiety. These differences in the exploratory pattern were confirmed to be influenced by genotype interaction with environmental novelty since the locomotor activity and total distance moved in the open field showed no significant difference between groups (n = 8 mice per group, P = 0.82, t test). In the elevated plus maze over a period of 5 min, no significant differences were observed between the WT and KO mice regarding distance, speed, or time spent in the open arm (Fig. 5*C*; n = 8 mice per group; distance, P = 0.65; speed, P = 0.57; time in open arm, P = 0.13; Mann-Whitney U tests). Nevertheless, the time spent in the center zone and the number of head dip events, both of which are indicative of increased

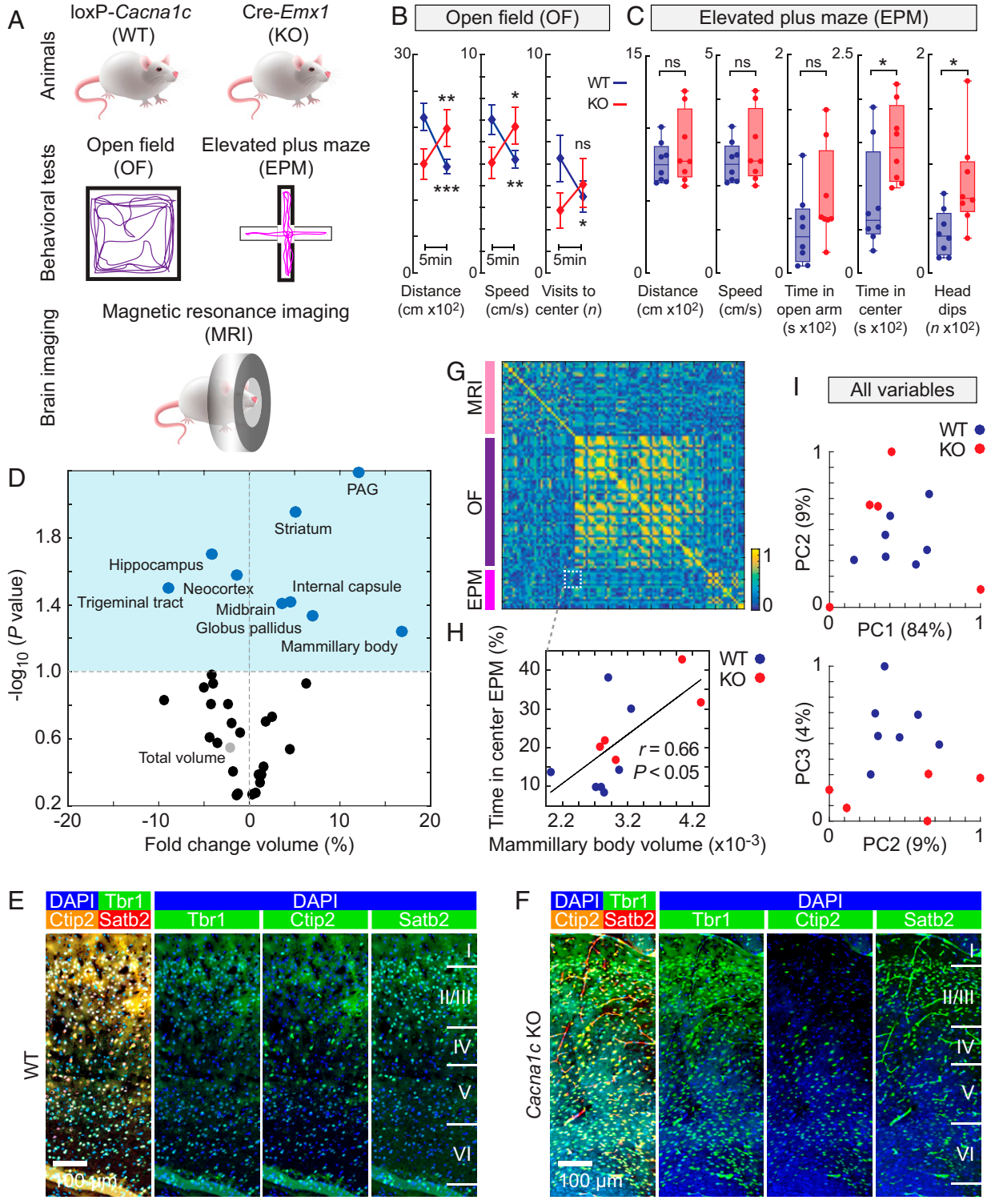

Fig. 5. *Cacna1c* KO mice exhibit abnormal brain anatomy and anxiety. (*A*) Experimental setups for the WT mice and the *Cacna1c* KO mice generated by Cre-Lox technology and used for the open-field (OF) and elevated plus maze (EPM) behavioral tests and MRI. (*B* and *C*) Quantification of the OF (*B*) and EPM (*C*) experiments for WT (blue, $n = 8$) and *Cacna1c* KO (red, $n = 8$) mice. Vertical bars represent SEM. For the box plots, the center line shows the median, the upper and lower boundaries of the box show the upper and lower quartiles, and the whiskers show the minimum and maximum values. (*D*) Volcano plot of the MRI-based volumetric measurements of 33 brain regions. The dark-blue dots indicate reduced and increased volumes, the light-gray dot indicates total brain volume, and the light-blue area indicates $P < 0.1$ after FDR correction. (*E* and *F*) Immunohistochemistry images of the somatosensory cortex in WT and *Cacna1c* KO mice. Somatosensory cortex was stained with Tbr1, Ctip2, and Satb2. Nuclei were detected using DAPI. (*G*) Correlation matrix for all variables measured in the EPM and OF tests and MRI. (*H*) Correlation between the mammillary body volume and the time spent in the center of the EPM behavioral test. The Pearson's *r* is stated. (*I*) Principal component (PC) analysis of all variables in *G* for the WT (blue, $n = 8$) and *Cacna1c* KO (red, $n = 8$) mice. The percentages of total variance explained by the first three axes (PC1, PC2, and PC3) are given in parentheses. The significance tests for the behavioral tests were calculated using two-way ANOVA with Bonferroni multiple comparisons. The *P* values for the volcano plot were calculated using unpaired two-tailed *t* tests. $*P < 0.05$, $**P < 0.01$, $***P < 0.005$; ns, nonsignificant ($P > 0.05$). (Scale bars, 100 µm.)

risk assessment behavior (48), were significantly increased 1.8-fold and 2.2-fold, respectively, in KO mice compared to WT mice (Fig. 5*C*; $n = 8$ mice per group; time in center, $P = 0.028$; head dip events, $P = 0.016$; Mann-Whitney U test). As expected from the univariate analyses, the principal component analysis showed a tendency of stronger clustering for open-field test variables than for those related to the elevated plus maze (*SI Appendix*, Fig. S7 *A* and *B*).

***Cacna1c* KO Mice Exhibit Abnormal Brain Anatomy but Normal Cortical Layering.** After the mouse behavioral experiments, we harvested the brains (WT: $n = 7$; *Cacna1c* KO: $n = 5$) for MRI scanning (Fig. 5*A*). Stacks of MRI images were aligned to a mouse brain atlas, and 33 regions were defined (*SI Appendix*, Movies S1–S3). Fold-changes and P values for comparisons between the WT and KO mice were calculated (Fig. 5*D*). There was no statistically significant change in the total brain volume (light-gray dot). However, there were statistically significant increases in the volumes of the periaqueductal gray (PAG), internal capsule, striatum, midbrain, globus pallidus and mammillary body as well as decreases in the volume of the hippocampus, neocortex, and trigeminal tract in the KO mice compared with those in the WT mice. Nevertheless, coronal brain sections immunostained with the cortical layer markers Tbr1, Ctip2, and Satb2 showed no significant difference in the thickness of the layers in the somatosensory cortex (WT: $n = 3$; *Cacna1c* KO: $n = 5$; layer I, $P = 0.70$; layer II/III, $P = 0.26$; layer IV, $P = 0.95$; layer V, $P = 0.37$; layer VI, $P = 0.56$; t tests) (Fig. 5 *E* and *F*; *SI Appendix*, Fig. S8). We then employed a multidimensional approach by merging all variables from the behavioral and MRI experiments, resulting in a total of 114 variables for each mouse. The correlation analysis revealed distinct clusters among groups of variables from the MRI, open-field, and elevated plus maze experiments (Fig. 5*G*). Interestingly, the volume of the mammillary bodies was positively correlated ($P < 0.05$, Pearson's $r = 0.66$) with the percentage of time spent in the center zone in the elevated plus maze experiment (Fig. 5*H*). Furthermore, there was a clear tendency of clustering in which the KO mice (red dots) tended to exhibit larger mammillary body volumes and longer times in the center. Additionally, the principal component analysis revealed the separation of WT and KO mice for all variables (Fig. 5*I*) and for variables from only the MRI data (*SI Appendix*, Fig. S7*C*). Taken together, our findings show that disruption of *Cacna1c* has an impact on the overall cerebral cortical development without disturbing normal cortical layering architecture.

Discussion

In this study, we show that forebrain-specific *Cacna1c* KO mice exhibit altered spontaneous Ca^{2+} activity in the developing neocortex as well as increased anxiety-like behavior and a disturbed brain structure in adult mice. Neural progenitor cells in the developing brain require normal expression levels of *Cacna1c* to modulate spontaneous electrical and Ca^{2+} activity. On the basis of computational modeling, patch-clamp recordings, and RT-qPCR, we propose a model of spontaneous network activity driven by functional pacemakers.

One recent mouse study showed that the embryonic deletion of *Cacna1c* in the forebrain glutamatergic neurons resulted in hippocampus dependent cognitive deficits (water cross maze), increased anxiety (in the dark-light test box), and reduced sociability (three-chamber sociability and social novelty tests) (49). This finding is partially in line with our results, although we knocked out *Cacna1c* in Emx1 cells and not in Nex cells. In mouse studies, Emx1 was found to be expressed in derivatives of the lateral, dorsal, and medial pallium, including the neocortex and hippocampal structures (50). However, only a subset of cells in ventral pallium–derived structures (for example, part of the amygdala) are Emx1 positive. Little expression of Emx1 is found outside the telencephalon, although a small number of scattered cells are found in the hypothalamus and PAG. Human MRI studies have shown that regional brain volume changes are common in patients with psychiatric disorders, including autism, attention deficit/hyperactivity disorder, bipolar disorder, and schizophrenia (reviewed in Ref. 51). In our animal experiments using MRI, we observed significant increases in the volume of several brain areas associated with anxiety [i.e., the PAG (52), striatum (53), and mammillary bodies (54)]. By combining MRI with behavioral assays, we revealed a correlation between the volume of the mammillary bodies, which are a region known to regulate state-dependent apprehension by alternating cortical oscillations (55), and the time spent in the center zone of the elevated plus maze, a behavior that reflects a motivational conflict (33). Relevant to our results, one study specifically investigated the volumes of the hypothalamus and mammillary bodies in patients with schizophrenia and healthy controls (54). In the patients, these brain structures were increased in volume. Intriguingly, the size of the mammillary bodies was inversely correlated with negative symptoms and directly correlated with anxiety. In rodents, lesions of the mammillary bodies result in increased exploratory behavior and thus decreased anxiety in both the elevated plus maze (56) and open-field tests (57).

Changes in regional brain volume could be due to mechanisms regulating proliferation, differentiation, migration, and apoptosis. In the embryonic mouse cortex, a gain-of-function *Cacna1c* mutation found in Timothy syndrome, an autosomal dominant multisystem disorder exhibiting syndromic autism, has been reported to result in Ca^{2+}-dependent differentiation defects that influence the abundance of neural progenitors (58). The Timothy syndrome–associated gain-of-function *Cacna1c* mutation was also shown to impair the radial migration of layer 2/3 excitatory neurons (59). Knocking out *Cacna1c* resulted in cortical neurons with a reduced total neurite length. The maturation of oligodendrocytes can also be affected by dysfunctional L-type VGCC signaling. Postnatal KO of *Cacna1c* caused a significant hypomyelination (60), whereas the Timothy syndrome–associated gain-of-function *Cacna1c* mutation produced a more complex morphology and higher levels of myelin protein expression (61). These reports and others underscore the crucial developmental impacts of L-type VGCC signaling in cortical development. Intriguingly, *Cacna1c* appears to be up-regulated in the cortical intermediate zone to stimulate spontaneous Ca^{2+} oscillations in neural progenitors and radial migration (62). Our group has previously shown that neural progenitors in the embryonic mouse cortex organize in small-world networks driven by spontaneous Ca^{2+} activity (28). Inhibiting these functional networks by blocking gap junctions affected neural progenitor proliferation and embryonic cortical layer formation. The results shown here suggest that *Cacna1c* knockdown affects the volume of specific brain regions, including the neocortex, while the thickness of the somatosensory cortical layers remains unaffected. The difference in these results may be due to technical limitations of the MRI and the histochemistry methods used to assess the neocortex volume and layer formation, respectively. However, the difference can also be explained by imbalances in proliferation and apoptosis in the *Cacna1c* knockdown animals. Interestingly, spontaneous Ca^{2+} oscillations in the developing brain have been shown to regulate the activity of caspase-3 (29), the final effector of the mitochondrial apoptotic pathway. Down-regulation of *Cacna1c* promoted mitochondrial resilience, enhanced resistance against apoptosis, and reduced the proliferation of neuronal cells (63).

In the computational model presented in this study, the only difference between functional pacemakers and nonpacemakers was the VGCC conductance. Intriguingly, this finding implies

that there is no need for specialized cells to act as pacemakers; instead, this function is due to a difference in the expression or conductance of VGCCs. The bifurcation analysis for VGCC conductance revealed two Hopf bifurcations, indicating that there is a *Cacna1c* expression window wherein spontaneous Ca^{2+} oscillations are evoked. This suggests that marginal differences in VGCC conductance, e.g., 20 μS/cm^2 versus 17.5 μS/cm^2 (Fig. 2 *B* and *C*), can activate or deactivate spontaneous Ca^{2+} oscillations, perhaps dynamically back and forth. When the connectivity of neural progenitors was analyzed, only a small fraction of the cells had both hub cell and pacemaker cell properties. In line with this result, it has been shown that network controllability mainly depends on nonhub nodes (64). Central to our model are pacemaker cells that exhibit spontaneous Ca^{2+} activity without the influence of adjacent cells, as supported by experiments in which some cells continued to oscillate under octanol treatment. Interestingly, a previous model of subthreshold membrane potential oscillations in inferior olivary neurons assumed the absence of pacemaker cells (65). By strongly coupling nonspontaneously oscillating cells, oscillations emerge as the new average parameter values force the system through a Hopf bifurcation. This model does not include Ca^{2+} per se, but the membrane potential is dependent on a low-voltage–activated VGCC (similar to a T-type channel) as well as a leakage current. Intriguingly, the expression of genes encoding T-type VGCCs also increases during the differentiation of neural progenitors (29, 66). Although *Cacna1d* was not up-regulated here, $Ca_v1.3$ L-type channels may still be of importance in analogy to adrenal chromaffin cells, where they function in concert with $Ca_v1.2$ channels (67). In a mouse model of Timothy syndrome, the G406R mutation in *Canca1c* on exon 8 coding for the IS6-helix of the $Ca_v1.2$ channel resulted in drastic changes in the action potential firing of adrenal chromaffin cells (68). It remains a question for future studies to analyze the effect of combining various L- and T-type VGCCs in a model similar to this one.

In conclusion, the forebrain-specific knockdown of *Cacna1c* leads to increased anxiety as well as structural changes in several brain regions, including the hippocampus, PAG, and mammillary bodies, in conjunction with disturbed spontaneous Ca^{2+} activity. We propose a theoretical framework in which spontaneous activity is driven by functional pacemaker cells expressing sufficient levels of *Cacna1c* connected to other cells with gap junctions. Surprisingly, our results suggest that a difference as small as one channel can determine whether a cell becomes a pacemaker cell, which implies that *Cacna1c* may act as a molecular switch that can determine the fate of neural progenitors. Although one channel may not be sufficient to reach a tipping point, our results demonstrate that subtle differences in expression at the single-cell level can have a major impact on a large scale. In summary, we present a possible mechanism by which the perturbed expression of *Cacna1c* during embryogenesis leads to inhibited spontaneous activity and thus disrupts neural development, thereby increasing susceptibility to subsequent psychiatric disease.

Data Availability. All study data are included in the article and/or supporting information.

ACKNOWLEDGMENTS. This work was supported by the Swedish Research Council (grants 2013-3189, 2017-00815, and 2021-03108 to P.U.), the Swedish Brain Foundation (grants FO2017-0107, FO2018-0209, and FO2020-0199 to P.U.), the Swedish Cancer Society (grants CAN 2016-801, 19 0544 Pj and 19 0545 Us to P.U.), the Swedish Childhood Cancer Foundation (grants PR2018-0123 and PR2020-0124 to P.U.), the Linnaeus Centre in Developmental Biology for Regenerative Medicine, the Knut and Alice Wallenberg Foundation (grants CLICK and Research Fellow to P.U.), the Karolinska Institutet's KID doctoral program (E.S.), Psykiatrifonden (E.S.), and the European Molecular Biology Organization advanced research fellow (ALTF 596-2014 to R.A.R.) and co-funded by the European Commission FP7 (Marie Curie Actions, EMBOCOFUND2012, GA-2012-600394).

1. M. Ekman, O. Granström, S. Omérov, J. Jacob, M. Landén, The societal cost of bipolar disorder in Sweden. *Soc. Psychiatry Psychiatr. Epidemiol.* **48**, 1601–1610 (2013).
2. M. Ekman, O. Granstrom, S. Omerov, J. Jacob, M. Landen, The societal cost of schizophrenia in Sweden. *J. Ment. Health Policy Econ.* **16**, 13–25 (2013).
3. P. Lichtenstein *et al.*, Common genetic determinants of schizophrenia and bipolar disorder in Swedish families: A population-based study. *Lancet* **373**, 234–239 (2009).
4. Schizophrenia Psychiatric Genome-Wide Association Study Consortium, Genome-wide association study identifies five new schizophrenia loci. *Nat. Genet.* **43**, 969–976 (2011).
5. Psychiatric GWAS Consortium Bipolar Disorder Working Group, Large-scale genome-wide association analysis of bipolar disorder identifies a new susceptibility locus near ODZ4. *Nat. Genet.* **43**, 977–983 (2011).
6. P. F. Sullivan, M. J. Daly, M. O'Donovan, Genetic architectures of psychiatric disorders: The emerging picture and its implications. *Nat. Rev. Genet.* **13**, 537–551 (2012).
7. P. J. Harrison, Molecular neurobiological clues to the pathogenesis of bipolar disorder. *Curr. Opin. Neurobiol.* **36**, 1–6 (2016).
8. Cross-Disorder Group of the Psychiatric Genomics Consortium, Identification of risk loci with shared effects on five major psychiatric disorders: A genome-wide analysis. *Lancet* **381**, 1371–1379 (2013).
9. M. B. Clark *et al.*, Long-read sequencing reveals the complex splicing profile of the psychiatric risk gene CACNA1C in human brain. *Mol. Psychiatry* **25**, 37–47 (2020).
10. M. J. Berridge, Calcium signalling and psychiatric disease: Bipolar disorder and schizophrenia. *Cell Tissue Res.* **357**, 477–492 (2014).
11. S. Bhat *et al.*, CACNA1C (Cav1.2) in the pathophysiology of psychiatric disease. *Prog. Neurobiol.* **99**, 1–14 (2012).
12. M. Hörtenhuber *et al.*, Mapping genes for calcium signaling and their associated human genetic disorders. *Bioinformatics* **33**, 2547–2554 (2017).
13. J. W. Hell *et al.*, Identification and differential subcellular localization of the neuronal class C and class D L-type calcium channel alpha 1 subunits. *J. Cell Biol.* **123**, 949–962 (1993).
14. R. E. Dolmetsch, U. Pajvani, K. Fife, J. M. Spotts, M. E. Greenberg, Signaling to the nucleus by an L-type calcium channel-calmodulin complex through the MAP kinase pathway. *Science* **294**, 333–339 (2001).
15. I. A. Graef *et al.*, L-type calcium channels and GSK-3 regulate the activity of NF-ATc4 in hippocampal neurons. *Nature* **401**, 703–708 (1999).
16. D. Lipscombe, T. D. Helton, W. Xu, L-type calcium channels: The low down. *J. Neurophysiol.* **92**, 2633–2641 (2004).
17. P. Stein, V. Savy, A. M. Williams, C. J. Williams, Modulators of calcium signalling at fertilization. *Open Biol.* **10**, 200118 (2020).
18. M. J. Berridge, P. Lipp, M. D. Bootman, The versatility and universality of calcium signalling. *Nat. Rev. Mol. Cell Biol.* **1**, 11–21 (2000).
19. P. Uhlén, N. Fritz, E. Smedler, S. Malmersjö, S. Kanatani, Calcium signaling in neocortical development. *Dev. Neurobiol.* **75**, 360–368 (2015).
20. P. Uhlén, N. Fritz, Biochemistry of calcium oscillations. *Biochem. Biophys. Res. Commun.* **396**, 28–32 (2010).
21. E. Smedler, P. Uhlen, Frequency decoding of calcium oscillations. *Biochim. Biophys. Acta* **1840**, 964–969 (2013).
22. M. Le Bon-Jego, R. Yuste, Persistently active, pacemaker-like neurons in neocortex. *Front. Neurosci.* **1**, 123–129 (2007).
23. N. C. Spitzer, Electrical activity in early neuronal development. *Nature* **444**, 707–712 (2006).
24. A. G. Blankenship, M. B. Feller, Mechanisms underlying spontaneous patterned activity in developing neural circuits. *Nat. Rev. Neurosci.* **11**, 18–29 (2010).
25. S. Illes *et al.*, Intrinsically active and pacemaker neurons in pluripotent stem cell-derived neuronal populations. *Stem Cell Reports* **2**, 323–336 (2014).
26. F. Ciccolini *et al.*, Local and global spontaneous calcium events regulate neurite outgrowth and onset of GABAergic phenotype during neural precursor differentiation. *J. Neurosci.* **23**, 103–111 (2003).
27. N. Yamamoto, G. López-Bendito, Shaping brain connections through spontaneous neural activity. *Eur. J. Neurosci.* **35**, 1595–1604 (2012).
28. S. Malmersjö *et al.*, Neural progenitors organize in small-world networks to promote cell proliferation. *Proc. Natl. Acad. Sci. U.S.A.* **110**, E1524–E1532 (2013).
29. P. Rebellato *et al.*, The T-type Ca^{2+} channel $Ca_v3.2$ regulates differentiation of neural progenitor cells during cortical development via Caspase-3. *Neuroscience* **402**, 78–89 (2019).
30. A. A. Walf, C. A. Frye, The use of the elevated plus maze as an assay of anxiety-related behavior in rodents. *Nat. Protoc.* **2**, 322–328 (2007).
31. V. Carola, F. D'Olimpio, E. Brunamonti, F. Mangia, P. Renzi, Evaluation of the elevated plus-maze and open-field tests for the assessment of anxiety-related behaviour in inbred mice. *Behav. Brain Res.* **134**, 49–57 (2002).
32. S. A. Barnett, The *Rat: A Study* in *Behavior* (Univ. of Chicago Press, Chicago, ed. Rev., 1975).
33. R. J. Blanchard, D. C. Blanchard, Attack and defense in rodents as ethoexperimental models for the study of emotion. *Prog. Neuropsychopharmacol. Biol. Psychiatry* **13** (suppl.), S3–S14 (1989).

34. G. A. Johnson, E. Calabrese, A. Badea, G. Paxinos, C. Watson, A multidimensional magnetic resonance histology atlas of the Wistar rat brain. *Neuroimage* **62**, 1848–1856 (2012).
35. G. A. Johnson *et al.*, Waxholm space: An image-based reference for coordinating mouse brain research. *Neuroimage* **53**, 365–372 (2010).
36. M. Modat *et al.*, Fast free-form deformation using graphics processing units. *Comput. Methods Programs Biomed.* **98**, 278–284 (2010).
37. Q. L. Ying, M. Stavridis, D. Griffiths, M. Li, A. Smith, Conversion of embryonic stem cells into neuroectodermal precursors in adherent monoculture. *Nat. Biotechnol.* **21**, 183–186 (2003).
38. J. Vandesompele *et al.*, Accurate normalization of real-time quantitative RT-PCR data by geometric averaging of multiple internal control genes. Genome *Biol.* **3**, research0034.1 (2002).
39. E. Smedler, S. Malmersjö, P. Uhlén, Network analysis of time-lapse microscopy recordings. *Front. Neural Circuits* **8**, 111 (2014).
40. P. Uhlén, Spectral analysis of calcium oscillations. *Sci. STKE* **2004**, pl15 (2004).
41. M. Gulisano, V. Broccoli, C. Pardini, E. Boncinelli, Emx1 and Emx2 show different patterns of expression during proliferation and differentiation of the developing cerebral cortex in the mouse. *Eur. J. Neurosci.* **8**, 1037–1050 (1996).
42. O. N. Suslov, V. G. Kukekov, T. N. Ignatova, D. A. Steindler, Neural stem cell heterogeneity demonstrated by molecular phenotyping of clonal neurospheres. *Proc. Natl. Acad. Sci. U.S.A.* **99**, 14506–14511 (2002).
43. M. B. Johnson *et al.*, Single-cell analysis reveals transcriptional heterogeneity of neural progenitors in human cortex. *Nat. Neurosci.* **18**, 637–646 (2015).
44. C. P. Fall, E. S. Marland, J. M. Wagner, J. J. Tyson, *Computational Cell Biology (Interdisciplinary Applied Mathematics)* (Springer, 2002).
45. M. Breakspear *et al.*, A unifying explanation of primary generalized seizures through nonlinear brain modeling and bifurcation analysis. *Cereb. Cortex* **16**, 1296–1313 (2006).
46. H. J. Luhmann *et al.*, Spontaneous neuronal activity in developing neocortical networks: From single cells to large-scale interactions. *Front. Neural Circuits* **10**, 40 (2016).
47. B. Q. Mao, F. Hamzei-Sichani, D. Aronov, R. C. Froemke, R. Yuste, Dynamics of spontaneous activity in neocortical slices. *Neuron* **32**, 883–898 (2001).
48. R. J. Rodgers, A. Dalvi, Anxiety, defence and the elevated plus-maze. *Neurosci. Biobehav. Rev.* **21**, 801–810 (1997).
49. N. Dedic *et al.*, Cross-disorder risk gene CACNA1C differentially modulates susceptibility to psychiatric disorders during development and adulthood. *Mol. Psychiatry* **23**, 533–543 (2018).
50. J. A. Gorski *et al.*, Cortical excitatory neurons and glia, but not GABAergic neurons, are produced in the Emx1-expressing lineage. *J. Neurosci.* **22**, 6309–6314 (2002).
51. E. L. Dennis, P. M. Thompson, Typical and atypical brain development: A review of neuroimaging studies. *Dialogues Clin. Neurosci.* **15**, 359–384 (2013).
52. F. G. Graeff, M. C. Silveira, R. L. Nogueira, E. A. Audi, R. M. Oliveira, Role of the amygdala and periaqueductal gray in anxiety and panic. *Behav. Brain Res.* **58**, 123–131 (1993).
53. T. Lago, A. Davis, C. Grillon, M. Ernst, Striatum on the anxiety map: Small detours into adolescence. *Brain Res.* **1654** (Pt B), 177–184 (2017).
54. S. Tognin *et al.*, Enlarged hypothalamic volumes in schizophrenia. *Psychiatry Res.* **204**, 75–81 (2012).
55. J. Jiang, G. Y. Wang, W. Luo, H. Xie, J. S. Guan, Mammillary body regulates state-dependent fear by alternating cortical oscillations. *Sci. Rep.* **8**, 13471 (2018).
56. D. J. Beracochea, A. Krazem, Effects of mammillary body and mediodorsal thalamic lesions on elevated plus maze exploration. *Neuroreport* **2**, 793–796 (1991).
57. M. P. Santacana, R. Alvarez Peláez, P. Tejedor, Effect of the lesion of the mammillary bodies on the performance in the open field. *Physiol. Behav.* **9**, 501–504 (1972).
58. G. Panagiotakos *et al.*, Aberrant calcium channel splicing drives defects in cortical differentiation in Timothy syndrome. *eLife* **8**, e51037 (2019).
59. S. Kamijo *et al.*, A critical neurodevelopmental role for L-type voltage-gated calcium channels in neurite extension and radial migration. *J. Neurosci.* **38**, 5551–5566 (2018).
60. V. T. Cheli *et al.*, Conditional deletion of the L-type calcium channel Cav1.2 in oligodendrocyte progenitor cells affects postnatal myelination in mice. *J. Neurosci.* **36**, 10853–10869 (2016).
61. V. T. Cheli *et al.*, Enhanced oligodendrocyte maturation and myelination in a mouse model of Timothy syndrome. *Glia* **66**, 2324–2339 (2018).
62. S. I. Horigane *et al.*, Development of an L-type Ca(2+) channel-dependent Ca(2+) transient during the radial migration of cortical excitatory neurons. *Neurosci. Res.* **169**, 17–26 (2020).
63. S. Michels *et al.*, Downregulation of the psychiatric susceptibility gene *Cacna1c* promotes mitochondrial resilience to oxidative stress in neuronal cells. *Cell Death Discov.* **4**, 54 (2018).
64. Y. Y. Liu, J. J. Slotine, A. L. Barabási, Controllability of complex networks. *Nature* **473**, 167–173 (2011).
65. Y. Manor, J. Rinzel, I. Segev, Y. Yarom, Low-amplitude oscillations in the inferior olive: A model based on electrical coupling of neurons with heterogeneous channel densities. *J. Neurophysiol.* **77**, 2736–2752 (1997).
66. L. M. Louhivuori *et al.*, Role of low voltage activated calcium channels in neuritogenesis and active migration of embryonic neural progenitor cells. *Stem Cells Dev.* **22**, 1206–1219 (2013).
67. A. Marcantoni *et al.*, Loss of Cav1.3 channels reveals the critical role of L-type and BK channel coupling in pacemaking mouse adrenal chromaffin cells. *J. Neurosci.* **30**, 491–504 (2010).
68. C. Calorio *et al.*, Impaired chromaffin cell excitability and exocytosis in autistic Timothy syndrome TS2-neo mouse rescued by L-type calcium channel blockers. *J. Physiol.* **597**, 1705–1733 (2019).